Structural and optical properties of oxygen doped single crystal ZnTe grown by Multi-Tube Physical Vapour Transport

J.T. Mullins[1*], F. Dierre[1], D.P. Halliday[2], B.K. Tanner[2], I. Radley[1], Z. Kang[3], C.J. Summers[3]

[1]Kromek Ltd., Thomas Wright Way, Sedgefield TS21 3FD, UK

[2]Department of Physics, University of Durham, South Road, Durham DH1 3LE, UK

[3]School of Materials Science and Engineering, Georgia Institute of Technology, Atlanta, GA 30332-0245, USA

Abstract

Bulk single crystals of zinc telluride up to 10 mm thick have been grown by the Multi-Tube Physical Vapour Transport technique and doped, in-situ during growth, with oxygen. Following hetero-epitaxial nucleation and buffer growth on 100 mm diameter GaAs seed wafers, oxygen was introduced to the quartz growth envelope, using nitrous oxide as a precursor, via a novel gas injection system. Mass spectra from a residual gas analyser sampling the gases exiting the growth envelope indicated that the nitrous oxide had been cracked at the operating temperature of the furnace releasing oxygen into the growth region. The structural perfection of the grown crystals was assessed by synchrotron based X-ray diffraction measurements and found to be extremely high, improving significantly with distance from the seed. Rocking curve widths, measured from a 4 mm x 7 mm area, as low as 20 arc secs were observed. No evidence was found for a reduction in crystalline quality resulting from the incorporation of oxygen. Luminescence studies (4 – 300 K) showed strong red luminescence at 680 nm persisting up to room temperature indicating that oxygen had been incorporated substitutionally onto tellurium sites. This material is highly transparent at the red emission wavelength with absorption coefficients of approximately 2 cm^{-1}. Under alpha radiation from a ^{241}Am source, scintillation was observed from the doped material with approximately 12,700 photons/MeV and a full width at half height maximum of 27%. The material is a potential candidate for large volume scintillation based radiation detectors.

Keywords: bulk crystal growth, vapour transport, zinc telluride, oxygen doping, X-ray diffraction, optical properties

* Corresponding author: email: john.mullins@kromek.com, Tel: +44 (0)1740 626 060, ORCID ID: 0000-0001-8069-8434

1. INTRODUCTION

In addition to possible applications in intermediate bandgap photovoltaic devices [1], zinc telluride doped with oxygen has potential as a scintillator detector for high energy X and γ radiation. The strong red luminescence, centred at 680 nm, emanating from a deep centre created by oxygen substituting for tellurium [2,3] has been shown to give rise to efficient scintillation in thin film form [4,5]. ZnTe has the potential for high energy resolution due to having a smaller fundamental energy gap, 2.3 eV at room temperature, and significantly higher carrier mobilities than conventional scintillators. These two factors are, respectively, expected to increase the potential optical output and to reduce the effects of non-proportionality [6]. The red emission is well matched to silicon photodetectors and zinc telluride also has the advantages of a high average atomic number, fast decay time and low afterglow. Furthermore, in contrast to the alkali halides, ZnTe is not hygroscopic.

Extremely promising results have been obtained with polycrystalline scintillator screens illuminated with 17 keV X-radiation [7]. In order to be an efficient detector of high energy radiation, ZnTe:O is required to be produced in bulk (several cm^3) form and be optically highly transparent. In this paper we describe how 100 mm diameter single crystal zinc telluride boules, of high structural perfection up to 10 mm thick, have been grown using the Multi-Tube Physical Vapour Transport (MTPVT) technique [8]. Similarly to previously described growth of bulk CdTe [9] and (Cd,Zn)Te [10,11], growth was initiated hetero-epitaxially on 100 mm diameter {211}B and {001} oriented GaAs seed wafers. The structural properties of material, which was not intentionally doped, studied by high-resolution X-ray diffraction and imaging, has been reported previously [12]. Rocking curves from small areas, using Bragg planes which contained the growth direction, were broadened only moderately from the predicted perfect crystal values, indicating a dislocation density varying from 3.5×10^6 cm^{-2} close to the seed to 3.3×10^5 cm^{-2} far from it. This suggests that defects introduced during nucleation due to the lattice mismatch to the seed crystal were being grown out over distances of several mm. Planes perpendicular to the growth direction showed biaxial concavity, attributed to the ZnTe crystal bowing under tensile strain generated at the substrate-crystal interface due to the mismatch in thermal expansion coefficients between ZnTe and GaAs.

Oxygen was introduced into the MTPVT growth envelope in the form of nitrous oxide, N_2O, via a differential pumping system and its decomposition monitored by an in-situ residual gas analyser (RGA). Upon heating to the temperatures of growth, N_2O decomposes [13] to yield atomic oxygen, available for incorporation into the growing crystal, and the nitrogen molecule, N_2, which is stable at these temperatures and hence not expected to be incorporated. Grown boules of zinc telluride, either oxygen doped or nominally undoped, were characterized structurally by high resolution X-ray diffraction and imaging, and optically by transmission, luminescence and scintillation. Doping levels were determined by resistivity and Hall effect measurements together with secondary ion mass spectroscopy (SIMS). (For simplicity, we will hereafter refer to samples that were not intentionally doped as “undoped”.)

2. GROWTH AND DOPING

In essence, the MTPVT system comprises one or more vertically oriented source tubes connected by a demountable horizontal crossmember to a vertically oriented growth tube containing a pedestal on which the seed wafer is located as shown in Fig. 1(a). This growth envelope is fabricated from quartz and the vertical tubes and crossmember are independently heated. Flow restrictors between the source and growth regions effectively de-couple mass transport from the source – sink temperature difference. The entire system is enclosed in a high vacuum chamber which eliminates air, provides thermal insulation and also evacuates the growth envelope via a small annular gap between the pedestal and the growth tube. This arrangement lends itself to the controlled introduction of dopants either from a solid source in an additional source tube or, as in the present case, as a gaseous pre-cursor introduced in the same manner. Fig. 1(b) shows the arrangement used for the growth of oxygen doped ZnTe. The source tube contained polycrystalline ZnTe source material. Nitrous oxide was introduced into the quartz envelope from a source cylinder and regulator via two orifices in series which act as flow restrictors. The pressure in the interspace between the restrictors is monitored by a capacitance manometer and set by an oil sealed rotary pump equipped with a throttle valve controlled by a throttle valve controller. This allows the pressure between the restrictors to be maintained at a low value and hence the flow through the downstream restrictor to be controlled in the range 0 to 0.5 sccm using readily available 50 μm and 100 μm orifices. Bypass valves around the orifices facilitate initial evacuation of the pipe work. The mass flow of nitrous oxide was calibrated in a subsidiary experiment in which the main chamber pressure was determined as a function of interspace pressure. The chamber pressure together with the known pumping speed of the turbomolecular system pump then allowed the mass flow rate to be calculated and hence the mass flow rate as a function of interspace pressure to be determined. This system allowed the nitrous oxide flow rate to be controlled to a precision of better than 5×10^{-5} sccm. A Stanford Research Systems RGA200 residual gas analyser was fitted to the main chamber to monitor the gases evolved during operation and hence cracking of the nitrous oxide during growth. Table 1 details the masses monitored and the chemical species assigned.

Mass (amu)	**Assignment**
28	N_2, CO
32	O_2
18	H_2O
44	CO_2, N_2O
2	H_2

Table 1. Masses monitored using the RGA and their assignments.

Fig. 2 shows RGA traces recorded during pump-down and admittance of nitrous oxide with the system un-heated. These values are uncalibrated but serve as a measurement of relative changes in partial pressure of the species monitored. As the nitrous oxide flow is increased from 1.7×10^{-4} sccm to 4.5×10^{-2} sccm then reduced to zero, the measured partial pressures of masses 44, 28 and 32, attributed to nitrous oxide, molecular nitrogen and molecular oxygen respectively, increase from the baseline in proportion to the flow rate. The increases in nitrogen and oxygen partial pressures are due to cracking of the nitrous oxide in the RGA's ionizer.

Fig. 3 shows RGA traces for the masses given in Table 1 recorded during pump down and a ZnTe growth run including a doping staircase together with the nominal growth temperature

profile. During the initial ramp to growth temperature, the partial pressures of all species increased as the system outgassed and then reduced after the final growth temperature had been reached. Introduction of 4.5 x 10^{-3} sccm of nitrous oxide after approximately 1/3 of the growth period resulted in an increase in the partial pressures of nitrous oxide and nitrogen. Significantly, and in contrast to the un-heated case, the nitrogen pressure increased more than that of nitrous oxide and there was no evidence for an increase in oxygen. This suggests that the nitrous oxide was being cracked at the growth temperature and that the released oxygen was combining with the source material inside the growth envelope.

A photograph of a typical oxygen doped ZnTe boule is shown in Fig. 4. SIMS analysis of the oxygen content of the ZnTe was performed with a Cameca 4F SIMS system using a caesium ion beam. Care was taken to avoid charging of the highly resistive doped samples by appropriate choice of beam conditions and gold coating of the samples. By use of a test sample in which an undoped ZnTe die was implanted with 5×10^{14} cm^{-2} of oxygen at 120 keV, the sensitivity to oxygen was determined to be that better than 2×10^{16} atoms cm^{-3}. No oxygen concentration above background was detected in any doped samples tested. However, the luminescence and resistivity measurements, reported below, show that oxygen had been successfully incorporated substitutionally for tellurium.

3. STRUCTURAL PROPERTIES

High-resolution X-ray diffraction and imaging experiments were conducted on the Huber diffractometer at beamline B16 of the Diamond Light Source, Didcot, U.K., The beam was monochromated to 10keV by a pair of independently tuned 111 Si reflections. The imaging detector was a Photonic Science SCMOS camera with a pixel pitch of 3.25μm. Samples were cut with side faces parallel to the {110} orientation flat on the GaAs seeds which were (001) oriented for all of the samples reported in this section resulting in (001) oriented growth. They were lapped, then polished using a 3μm diamond suspension on fabric polishing pads and finally etched for two minutes in a solution of 2% bromine in methanol at 21°C to remove the residual strain associated with the polishing process. For consistency with the scintillation results, topographs (diffraction images) are reproduced here as negatives (with enhanced intensity shown lighter) looking towards the X-ray source. The incidence plane is always vertical and the seed end is on the right hand side of the images with the growth direction horizontal. All images shown here were taken using the surface symmetric 220 reflection.

The plane wave diffraction images of both doped and undoped crystals in which stable growth was achieved (Figs. 5(a) and (b)) showed a high degree of uniformity in the image, the image extending over most of the illuminated area. This latter observation implies that the misorientation across the specimen area was less than about one or two times 13 arc seconds. [The value of 13 arc secs, which represents the angular acceptance equivalent to the dispersion in the arrangement, arises from adding in quadrature the intrinsic reflecting range at 10keV of the 111 reflection of silicon (5.7 arc secs) and the intrinsic reflecting range of a perfect ZnTe crystal in the 220 reflection (11.5 arc secs)]. This assessment is supported by the 55 arc secs full width at half height maximum (FWHM) of the full beam rocking curve of the undoped crystal and 20 arc secs for the oxygen doped sample.

The rocking curve peak position taken with a 0.2 mm × 0.2 mm area beam (Fig 7(a)) varies monotonically with distance from the seed in both crystals shown in Fig 5, indicating that there

is a gradual reduction in the elastic strain associated with the mismatch between thermal expansion coefficients of ZnTe crystal and GaAs seed [12]. A corresponding improvement in lattice perfection is evidenced from the small beam area rocking curves as a function of position along the growth axis, the scan being horizontal from right to left referenced to Fig 5. Fig 7(a) shows such a sequence of rocking curves across the undoped sample of Fig 5(a). As one moves away from the region adjacent to the seed, the rocking curve FWHM decreases exponentially (Fig 7(b)). Far from the seed, the rocking curve FWHM is 18.7 arc secs, which, when the monochromator FWHM and the intrinsic FWHM of perfect ZnTe are subtracted in quadrature, gives a broadening of 13.7 arc secs. This is in good agreement with previous, limited, measurements on undoped MTPVT-grown ZnTe [12]. There are a number of models of varying complexity to relate rocking curve broadening to the dislocation density, but unless the dislocation configuration is known at least to some degree, a simple model giving an approximate value is adequate. According to the mosaic model of Hirsch [14] dislocation density ρ is related to the rocking curve broadening β by

$$\rho = \frac{\beta^2}{9b^2} \qquad (1)$$

where b is the Burgers vector. For the zincblende structured ZnTe we take the Burgers vector to be equal to $a/\sqrt{2}$ where a is the lattice parameter, giving a dislocation density of $2.6(\pm0.1)\times10^5$ cm^{-2} at the end of the crystal furthest from the seed. Adjacent to the seed this rises to $7.8(\pm0.1)\times10^6$ cm^{-2}. We find (Fig. 7(b)) that the dislocation density calculated using this model falls off exponentially with distance from the seed. The best fit curve gives a residual dislocation density at notionally large distance of 1.9×10^5 cm^{-2}. An exponential fit can be interpreted as a constant probability, in an increment of distance, that dislocations grow out or annihilate, a characteristic of stable growth. The dislocation density of the doped crystal shown in Fig 5(b) followed a similar exponential dependence to that shown in Fig 7(b), although with lower values of dislocation density.

On some occasions, unstable growth resulted. This instability did not appear to be directly related to the oxygen doping as similar instabilities were occasionally observed when no doping was undertaken and when an inert gas (argon) was flowed during growth. Furthermore, when a thick undoped buffer was grown prior to initiating any dopant flow, no features commensurate with the introduction of the dopant were observed. As illustrated in the X-ray data shown in Fig 8, in such cases there is no systematic trend in either the rocking curve position or FWHM after about 1mm from the seed, characteristic of unstable growth. Initially there is a systematic change in peak position, but now moving towards reduction in lattice parameter. This does not continue and after about 1 mm of growth, the rocking curve FWHM broadens and the peak positions become variable and often bimodal. As well as having much broader rocking curve widths, the monochromatic topographs of such crystals were much less uniform than crystals where stable growth was achieved (Fig 8(b)). It is likely that such growth instability results from poor nucleation although the possibility that the flow of gas in the system disturbs the growing crystal cannot be ruled out. The luminescence and scintillation properties of the doped crystals do not seem to be sensitive to the lattice perfection on the scale revealed in the topographs.

4. OPTICAL AND ELECTRICAL PROPERTIES

4.1. Transmission

A near infra-red transmission map of a 4 mm thick slice taken from the oxygen doped boule shown in Fig. 4 was taken using an Olympus BX51 microscope equipped with a silicon CCD camera, computer controlled stage and a software application which allowed the recording of a composite image (Fig. 9). Dark defects can be seen in the inset, adjacent to the seed, but away from the seed, the material is transparent and no dark defects can be detected.

Near band edge optical transmission spectra have been obtained at room temperature along the three orthogonal axes of rectangular prisms of undoped zinc telluride cut from the boules using a wire saw then mechanically polished. The transmission measurements were made over the wavelength range 500 - 800 nm using a Cary 5000 UV – vis - NIR spectrophotometer. The light beam was confined into a 1.5mm pinhole before passing through the sample. The prisms had dimensions of 3.8 × 5.2 × 25 mm and by fitting the three transmission spectra it was possible to separately extract internal losses and scattering and losses due to surface imperfections.

Internal absorption and scattering losses from the light beam may be represented by an expression of the form:

$$\frac{I}{I_0} = \exp(-\alpha d) \qquad (2)$$

where I is the intensity at a path length of d, I_0 is the initial intensity and α is a parameter characterizing absorption and scattering within the sample. Both α and the fractional scattering at each air / ZnTe interface, S, may be extracted from the transmission data by fitting, for the three different path lengths (length, width and height), to the following expression which takes multiple internal reflections into account:

$$T = \frac{\exp(-\alpha d).(1-R-S)^2}{1-R^2.(1-S)^2.\exp(-2\alpha d)} \qquad (3)$$

where T is the fractional transmission and R is the reflectance loss calculated from the refractive index. This expression and its derivation are essentially the same as the standard formula for transmission through a block but with an additional term, S, to take account of scattering at interfaces. The refractive index as a function of photon energy was calculated using the formula and parameters of Pikhtin and Yas'kov [15] and values of S and α obtained by curve fitting to the spectral data.

Performing this fitting at the emission wavelength of the oxygen centre, 680 nm, yields the results shown in Fig. 10 for six samples cut from the same boule and prepared with three different final surface polishes: grit sizes of 3 μm, 1 μm and 0.1 μm.

This analysis can be performed at each wavelength in the transmission spectra to yield internal absorption / scattering and interface scattering spectra separately as shown in Figs. 11 and 12.

It can be seen that, at the wavelength of the oxygen related emission, internal absorption and scattering losses are very low at ~ 2 cm^{-1}. As expected, surface scattering is reduced at longer wavelengths (lower photon energies) and as the quality of the surface polishing is improved, using finer grit sizes.

II-VI compounds typically exhibit an exponential absorption tail below the fundamental gap as described by the empirical expression of Urbach [16]. The solid line on the absorption spectrum is a fit to Urbach's expression:

$$\alpha = \alpha_0 \exp(h\nu - E_0)/\beta) \qquad (4)$$

for the sub-gap absorption tail. α is the absorption coefficient, α_o is the absorption coefficient extrapolated to the band gap energy, $h\nu$ is the photon energy, E_0 is the band gap and β is a parameter quantifying the energy spreading of the absorption below the bandgap. The 298K energy gap was taken to be [17] 2.295 eV. Fitting Equation 4 to the region of exponential absorption yields a value of 11.5 meV for β.

Fourier Transform infra-red transmission (FTIR) spectra obtained over the 2 - 25 μm range from doped and undoped material are shown in Fig. 13. A Thermo Scientific Nicolet 6700 FT-IR system was used for these measurements. It can be seen that for the doped samples the transmission is approximately constant at approximately 63% for wavelengths < 20 μm. This is as expected for a material with the refractive index of ZnTe and low internal losses. Nahory and Fan [18] have attributed infra-red absorption at wavelengths > 20 μm in ZnTe to multi-phonon absorption. The TO phonon in ZnTe has an energy of 25.4 meV therefore two phonon absorption would be expected to occur at approximately 24 μm as observed in this material. In contrast the material which was undoped shows increasing absorption with wavelength for wavelengths < 20 μm which is likely to be due to free carrier absorption.

4.2. Luminescence and electrical measurements

Prior to undertaking photoluminescence studies, polished ZnTe:O dice were etched in a bromine / methanol solution in order to remove polishing damage. Samples were mounted in a 4 K closed cycle cryostat. Luminescence was excited using the 514 nm line of an Ar^+ laser. Luminescence emission spectra were recorded using a grating spectrometer coupled to a cooled Si photodiode array. Figs. 14(a) and (b) show temperature dependent photoluminescence spectra for respectively, undoped and oxygen doped ZnTe. It can be seen that, for undoped material at low temperature, the luminescence is dominated by exciton-related near band edge emission centred at 2.35 eV, while for the oxygen doped material the broad red emission around 680 nm (1.82 eV) associated with the oxygen centre [2] dominates. Such red emission has been seen in thin film ZnTe doped with oxygen [1]. The thermal activation of photoluminescence emission can be fitted to a bi-exponential function of the form:

$$I(T) = \frac{I_0}{1 + \alpha_1 \exp(-E_1 / k_B T) + \alpha_2 \exp(-E_2 / k_B T)} \qquad (5)$$

where E_1 and E_2 are independent energies of thermal activation of carriers out of the radiative transition ground and excited states to a higher energy non-radiative energy level thereby quenching the luminescence. The parameters α_1 and α_2 are a measure of the degeneracy of the non-radiative levels relative to the radiative levels. This model has been shown to correctly simulate the temperature dependence of luminescence transitions [19,20]. The integrated

luminescence intensity for the two samples is plotted as a function of inverse temperature in Fig. 15. The fitted lines use the relationship (5) above and the parameters given in Table 2.

	Undoped	**O Doped**
α_1 (a.u.)	3.44	1.66
α_2 (a.u.)	102	760 x 10^6
E_1 (meV)	4.08	5.02
E_2 (meV)	29.2	504

Table 2. Parameters used in Equation 5 to fit the temperature dependent luminescence data shown in Fig. 13.

Illumination and light collection were identical for both samples and therefore their intensity scales are comparable. It can be seen that the doped sample exhibits significantly brighter luminescence and furthermore, this luminescence is not quenched as strongly as the near band edge emission as the temperature increases. This is a consequence of the significantly higher activation energy for the quenching of the luminescence from the oxygen related states. It can be seen that, for O doped material, the activation energy E_2 is 504 meV, close to the difference between the energy of the oxygen level (1.82 eV) and the fundamental energy gap of ZnTe (2.3 eV). This provides further evidence of the origin of this PL emission band being related to O doping. This behaviour is also consistent with the very long observed radiative lifetimes in excess of 1 μs associated with oxygen states [19]. Theoretical studies have confirmed that carriers in deep level oxygen states recombine via intermediate band states [22]. Our observed luminescence behaviour is compatible with this model. As indicated by the absence of free carrier absorption in the doped samples, this confirms that the material had, indeed, been doped with oxygen and that the oxygen had been incorporated substitutionally for tellurium. Further confirmation that the material had indeed been successfully doped was provided by resistivity and Hall effect measurements. Typical undoped material was found to be p-type with a resistivity of 31 Ωcm and a mobility of 74 $cm^2V^{-1}s^{-1}$ by current voltage and Hall effect measurements. In contrast contactless resistivity measurements made using a SemiMap COREMA-WT resistivity mapper showed that the resistivity of oxygen doped material was > 10^{12} Ωcm. This indicates that the Fermi energy had been pinned deep in the fundamental gap by traps created by the oxygen deep level state.

Under X-ray or alpha particle irradiation, the oxygen doped material exhibits scintillation. Fig. 16 shows a CCD camera image taken of a 10 x 2 mm face of a 10 x 10 x 2 mm ZnTe die while another perpendicular face was being irradiated by 60 keV X-rays. The geometry is shown in the inset. By calculating the attenuation profile of 60 keV X-ray in ZnTe, it is found that 90% X-rays will be absorbed in 0.7 mm. Therefore, the X-ray excitation could not go through the whole sample thickness of 2 mm and only one side emits scintillation light as demonstrated in Fig.16. To estimate the light output yield, alpha particle scintillation experiments were also performed. An ^{241}Am alpha particle point source was placed directly on top of the scintillator samples for the counting measurements. The opposite side of the sample was covered with optical grease for effective light coupling and pressed onto a photomultiplier tube (R960 Hamamatsu PMT) with extended detection range in the red for effective light transfer. The pulse height spectrum of a 10 x 10 x 2 mm^3 ZnTe die is shown in Fig. 17. The full width at half maximum was determined to be 27%. By comparing the peak channels with that of a

commercial 10 x 10 x 5 mm^3 CsI:Tl scintillator with typical light output of 54,000 photons/MeV tested under equivalent conditions, the light output of the oxygen doped ZnTe was estimated to be ~12,700 photons/MeV. The quantum efficiency response of the PMT at different wavelengths (680nm for ZnTe:O and 550nm for CsI:Tl) was considered for this estimation.

5. DISCUSSION AND CONCLUSION

Luminescence spectra indicate that oxygen had been incorporated into ZnTe, substitutionally for tellurium, to create the well-known red emission. Electrical measurements showing greatly increased resistivity also support the creation of a deep level. However, although the optical data demonstrates that oxygen is incorporated, SIMS analysis failed to detect oxygen above the detection limit of better than 2×10^{15} cm^{-3}. Given the known transport rate of approximately 4 gh^{-1} and a N_2O flow rate of 4.5×10^{-2} sccm, had all the supplied oxygen been incorporated it would have been present at a concentration of ~ 0.3 at%. It is likely, therefore, that oxygen is reacting with zinc in the vapour to form zinc oxide. This hypothesis is supported by the observation of deposits of zinc oxide, which has a significantly lower vapour pressure than ZnTe, on the quartz-ware upstream of the growth region at the end of growth runs. Despite the very low dopant concentration, scintillation light output was approximately one quarter of that of CsI:Tl, a well-developed commercially available scintillator. Increasing the oxygen concentration would probably lead to a much greater light output. When stable growth was achieved, the lattice perfection of the doped crystals was comparable with the undoped ones. It is likely that instability sometimes observed in the growth originates from poor nucleation although the possibility that the gas flow associated with the dopant precursor is disrupting the growth cannot be completely ruled out.

In conclusion, single crystal zinc telluride has been successfully doped with oxygen in-situ during bulk vapour growth using nitrous oxide. The best material grown has high crystal lattice uniformity and exhibits strong red luminescence at room temperature. It has been shown to be highly transparent with internal losses as low as 2 cm^{-1}. The latter is a pre-requisite for large volume scintillator detectors. For the present process, oxygen incorporation appears, however, to be limited by pre-reaction in the vapour phase during growth and that the efficiency of the red luminescence. In order to increase the oxygen concentration and hence the luminescence efficiency, further development is required to reduce the extent of pre-reaction. This may be by, for example, reducing the concentration of zinc in the vapour by controlling the vapour stoichiometry or by shortening the path length for oxygen inside the growth envelope.

ACKNOWLEDGMENT

This work has been supported by the US Department of Homeland Security, Domestic Nuclear Detection Office, under competitively awarded contract HSHQDC-13-C-B0022. This support does not constitute an express or implied endorsement on the part of the Government. Sincere thanks are expressed to Ian Pape, Igor Dolbnya, Kawal Sawhney and Andrew Malandain of beamline B16 at the Diamond Light Source for their excellent technical support.

REFERENCES

[1] W. Wang, A.S. Lin and J.D. Phillips, Appl. Phys. Lett. **95** 011103 (2009)

[2]J.L. Merz, Phys. Rev. **176** 961 (1968).

[3]J.J. Hopfield, D.G. Thomas, R.T. Lynch, Phys. Rev. Lett. **17** 312 (1966)

[4]Z.T. Kang, C.J. Summers, H. Menkara, B.K. Wagner, R.Durst, Y. Diawara, G. Mednikova, T. Thorson, Appl. Phys. Lett. **88** 111904 (2006)

[5]V.V. Nagarkar, V. Gaysinskiy, O.E. Ovechkina, S. Miller, B. Singh, Guo Liang, T. Irving, IEEE Trans. Nucl. Sci. **57** 923 (2010).

[6]W.W. Moses, G.A. Bizarri, R.T. Williams, S.A. Payne, A.N. Vasil'ev, J. Singh, Q. Li, J.Q. Grim, W.S. Choong, IEEE Trans. Nucl. Sci. **59** 2038 (2012).

[7] Z.T. Kang, H. Menkara, B.K. Wagner, C.J. Summers, R. Durst, Y. Diawara, G. Mednikova and T. Thorson, J Electron. Mater. **35** 1262 (2006)

[8]J.T. Mullins, J. Carles, N.M. Aitken, A.W. Brinkman, J. Cryst. Growth **208** 211 (2000).

[9]J.T. Mullins, B.J. Cantwell, A. Basu, Q. Jiang, A. Choubey, A.W. Brinkman, J. Cryst. Growth **310** 2058 (2008).

[10]J.T. Mullins, B.J. Cantwell, A. Basu, Q. Jiang, A. Choubey, A.W. Brinkman, B.K. Tanner, J. Electron. Mater. **37** 1460 (2008).

[11]A. Choubey, V. Perumal, A.T.G. Pym, J. T. Mullins, P. J. Sellin, A.W. Brinkman, I. Radley, A. Basu, B.K. Tanner, J. Cryst. Growth **352** 120 (2012).

[12]J.T. Mullins, F. Dierre, B.K. Tanner, J. Cryst. Growth **413** 61 (2015).

[13]H.S. Johnston, J. Chem. Phys. **19** 663 (1951).

[14] P.B. Hirsch, "Mosaic structures", Ch. 6 in: B. Chalmers, R. King (Eds.), Prog. In Metal

Physics, Pergamon Press, New York, (1956).

[15]A.N. Pikhtin, A.D. Yas'kov, Sov. Phys. Semicond. **22** 613 (1988).

[16]F. Urbach, Phys. Rev. **92** 1324 (1953).

[17]K.P. O'Donnell, P.G. Middleton in EMIS Datareview Series No. 17 "Wide Bandgap II-VI Semiconductors" Ed. R. Bhargava INSPEC 1997.

[18]R.E. Nahory, H.Y. Fan, Phys. Rev. **156** 825 (1967).

[19]D. Bimberg, M. Sondergeld, E. Grobe, Phys. Rev. **B4**, 3451 (1971).

[20]D.P. Halliday, M.D.G. Potter, J.T. Mullins, A.W. Brinkman, J. Cryst. Growth **220** 30 (2000).

[21]Wang, W.M., A.S. Lin, J.D. Phillips, and W.K. Metzger, Appl. Phys. Lett., **95** 261107 (2009).

[22]C. Tablero, A. Marti, A. Luque, Appl. Phys. Lett., **96** 121104 (2010).

Figure Captions

FIG. 1. (a) Schematic of the MTPVT system employed for the growth of ZnTe. (b) Gas circuit of the MTPVT system and gas inlet.

FIG. 2. Partial pressures recorded inside the MTPVT vacuum jacket during admittance of nitrous oxide into the growth envelope with all heating elements cold. These values are uncalibrated.

FIG. 3. Partial pressures recorded inside the MTPVT vacuum jacket during a ZnTe growth run which incorporated an oxygen doping staircase. These values are uncalibrated.

FIG. 4. Photograph of a 100 mm diameter, 2.5 mm thick oxygen doped ZnTe boule.

FIG. 5. Plane wave diffraction images (topographs) of (a) an undoped ZnTe crystal, field width 6 mm and (b) an oxygen doped crystal, field width 7 mm.

FIG. 6. Large beam area (4mm × 7 mm), high resolution diffraction rocking curves from (a) the undoped ZnTe crystal of Fig 4(a) and (b) the doped crystal of Fig 4(b).

FIG. 7. (a) Rocking curves from 0.2×0.2 mm^2 area beam for various distances from the seed along an undoped crystal. (b) Dislocation density, calculated from the rocking curve FWHM, as a function of distance from seed. Solid line is an exponential fit to the data.

FIG. 8. (a) Small beam area rocking curves, at various distances from the seed, from an oxygen doped crystal in which stable growth was not achieved. (b) Monochromatic X-ray topograph of a crystal grown under high N_2O flow rate in which stable growth was not achieved. Field width 5 mm.

FIG. 9. Near infra-red transmission map of a slice taken from the oxygen doped ZnTe boule. The inset is a magnified view of the dark defects near the seed. (The grid lines are artefacts of the image stitching software.)

FIG. 10. Optical transmission at 680 nm for six samples of undoped ZnTe.

FIG. 11. Absorption spectra of undoped ZnTe. The solid line is given by Equation 4 with $\alpha = 10^4$ cm^{-1}, $E_0 = 2.295$ eV and $\beta = 11.5$ meV.

FIG. 12. Surface scattering spectra of undoped ZnTe. Data for six samples are shown; two for each grit size.

FIG. 13. FTIR spectra for three oxygen doped and two undoped ZnTe crystals. The doped crystal was 5 mm thick and the undoped 3.8 mm.

FIG. 14. Temperature dependent photoluminescence spectra of (a) undoped and (b) oxygen doped ZnTe.

FIG. 15. Temperature dependence of integrated emission intensity for nominally undoped and oxygen doped ZnTe.

FIG. 16. Scintillation from oxygen doped ZnTe under 60 keV X-ray irradiation.

FIG. 17. ^{241}Am spectrum for oxygen doped ZnTe.

Fig. 1

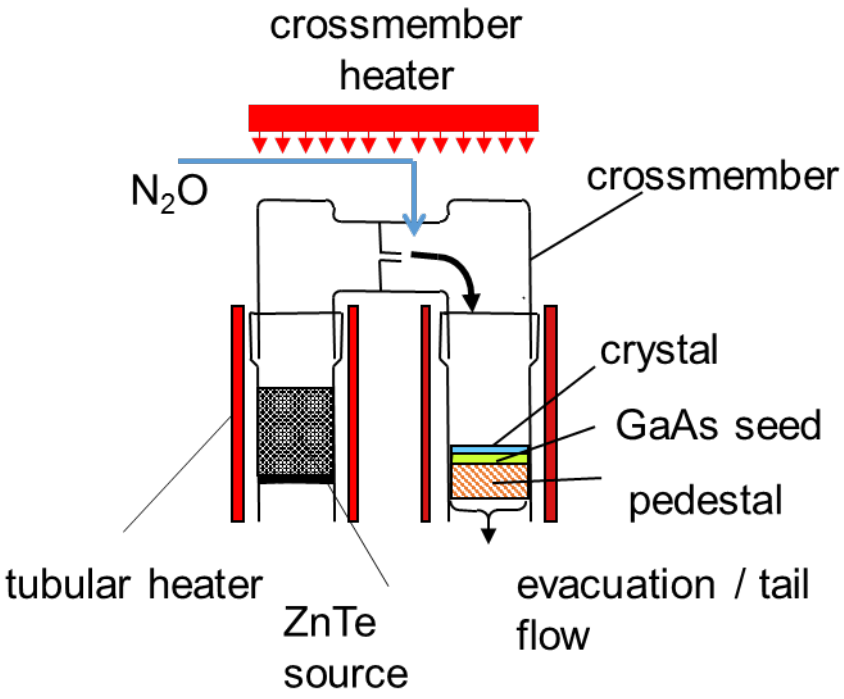
crossmember
heater
N_2O
crossmember
crystal
GaAs seed
pedestal
tubular heater
ZnTe
source
evacuation / tail
flow

(a)

Fig. 1

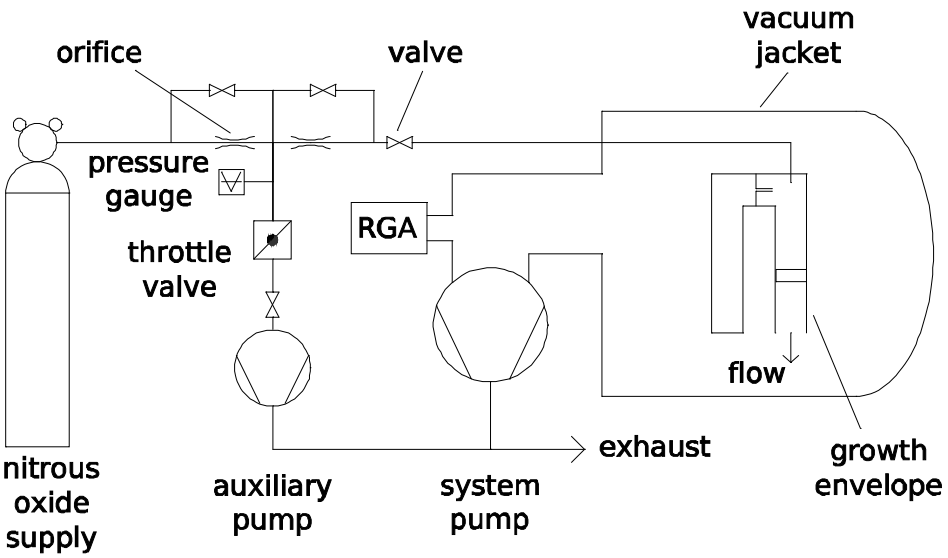
orifice
valve
vacuum jacket
pressure gauge
throttle valve
RGA
flow
exhaust
growth envelope
nitrous oxide supply
auxiliary pump
system pump

(b)

Fig. 2

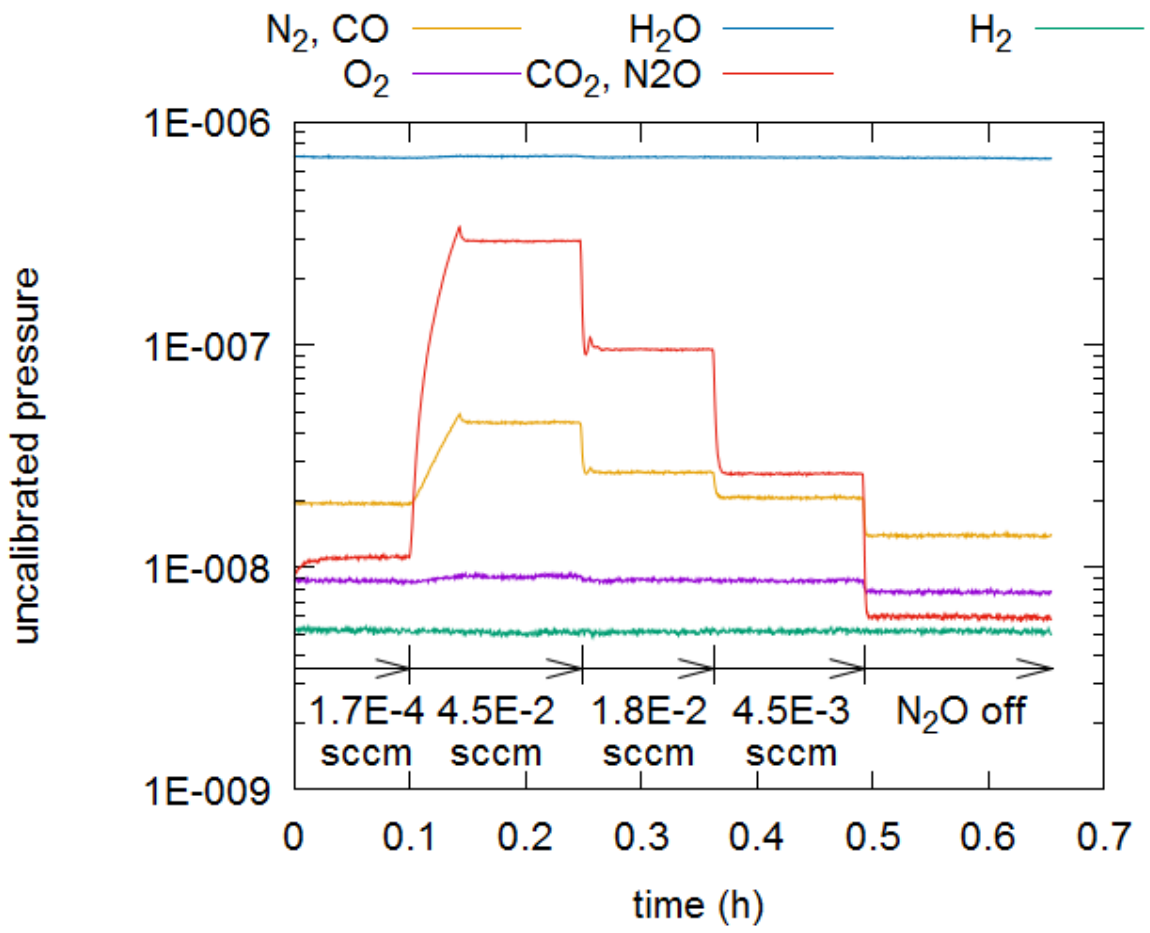
N2, CO
H2O
H2
O2
CO2, N2O
uncalibrated pressure
1E-006
1E-007
1E-008
1E-009
1.7E-4 sccm
4.5E-2 sccm
1.8E-2 sccm
4.5E-3 sccm
N2O off
0
0.1
0.2
0.3
0.4
0.5
0.6
0.7
time (h)

Fig. 3

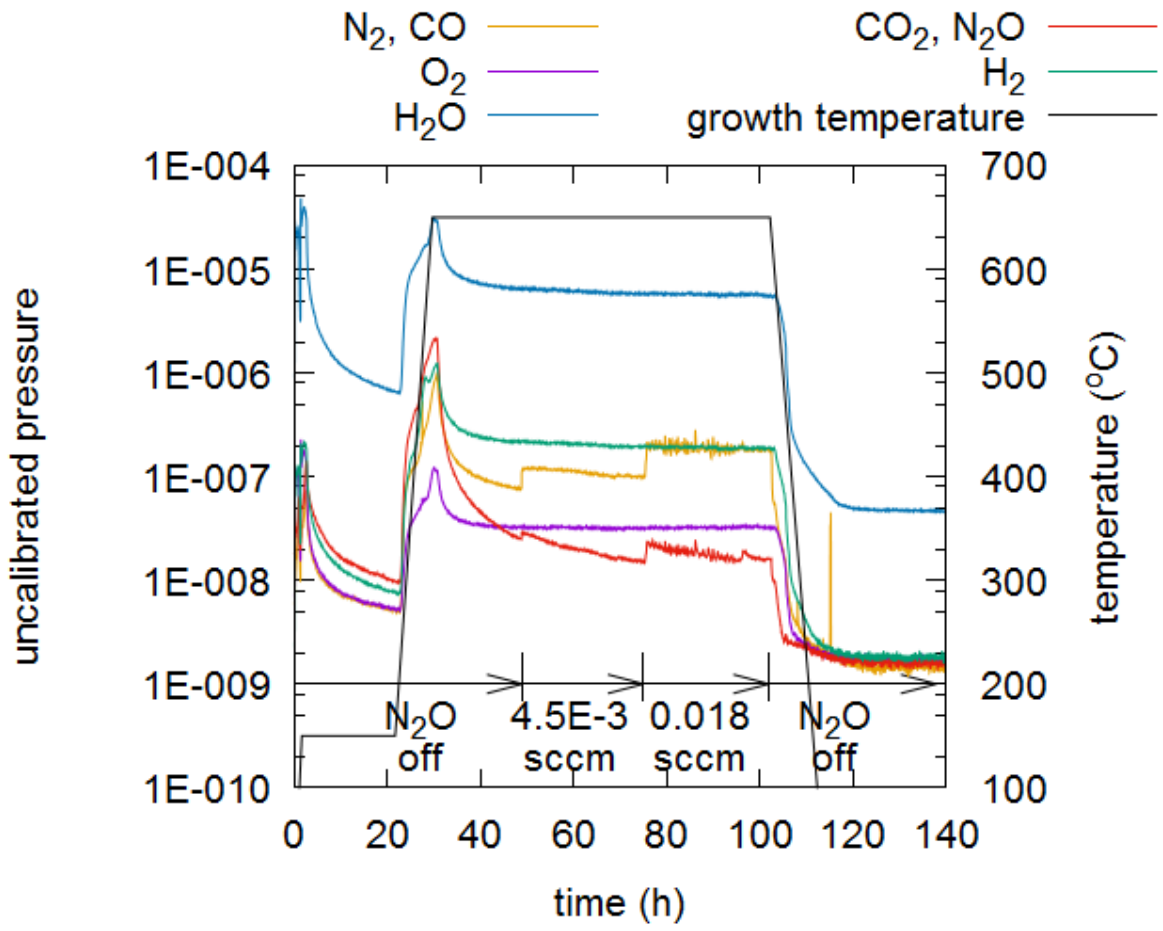
N2, CO
O2
H2O
CO2, N2O
H2
growth temperature
uncalibrated pressure
temperature (°C)
1E-004
1E-005
1E-006
1E-007
1E-008
1E-009
1E-010
700
600
500
400
300
200
100
0
20
40
60
80
100
120
140
time (h)
N2O off
4.5E-3 sccm
0.018 sccm
N2O off

Fig. 4

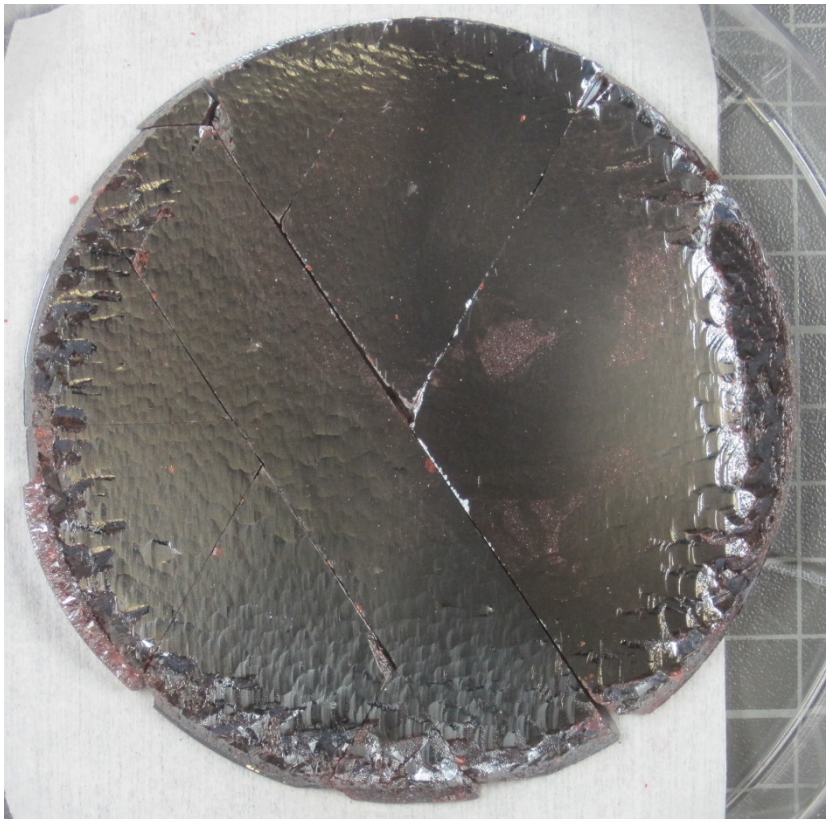

Fig. 5

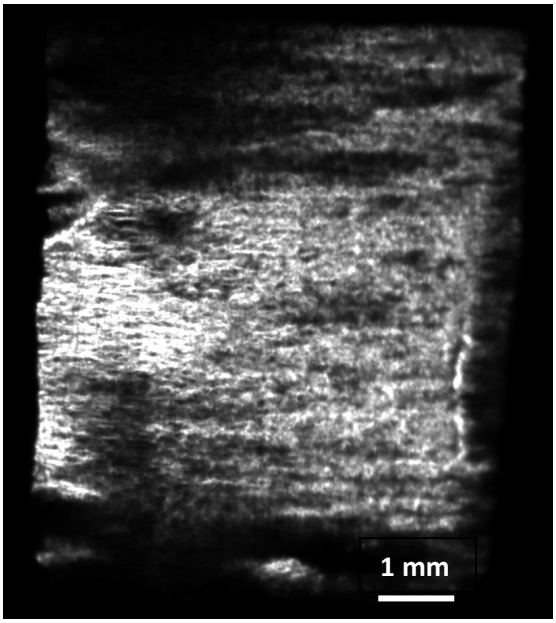

(a)

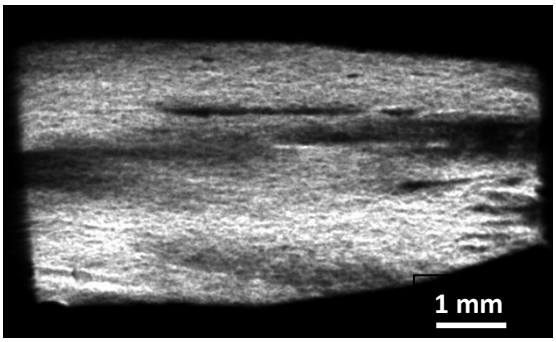

(b)

Fig. 6

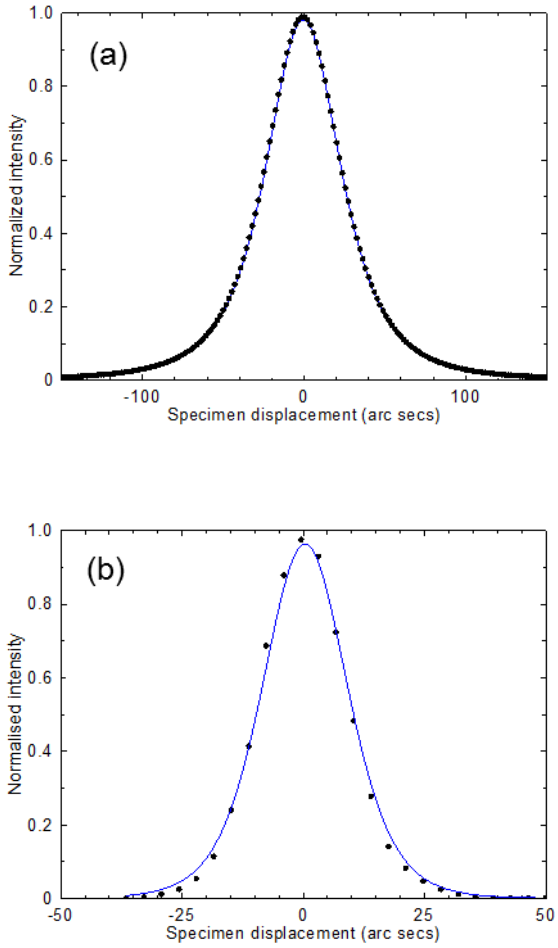
(a)
Normalized intensity
1.0
0.8
0.6
0.4
0.2
0
-100
0
100
Specimen displacement (arc secs)
(b)
Normalised intensity
1.0
0.8
0.6
0.4
0.2
0
-50
-25
0
25
50
Specimen displacement (arc secs)

Fig. 7

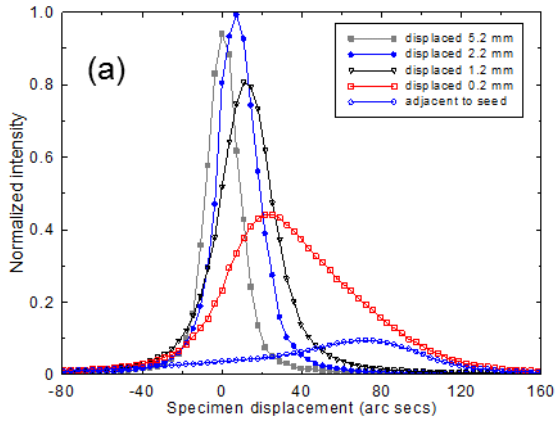
(a)
displaced 5.2 mm
displaced 2.2 mm
displaced 1.2 mm
displaced 0.2 mm
adjacent to seed
Normalized intensity
Specimen displacement (arc secs)
1.0
0.8
0.6
0.4
0.2
0
-80
-40
0
40
80
120
160

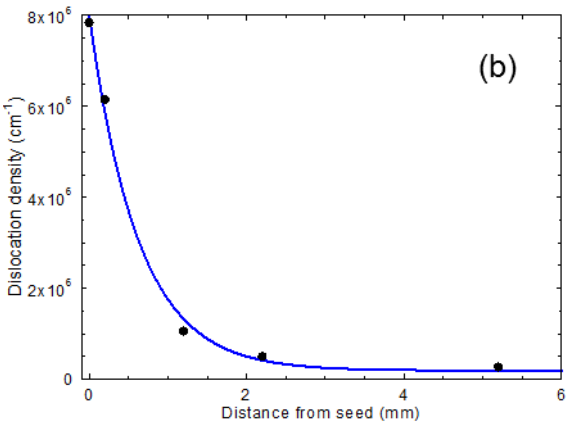
(b)
Dislocation density (cm^{-1})
Distance from seed (mm)
8x10^6
6x10^6
4x10^6
2x10^6
0
0
2
4
6

Fig. 8

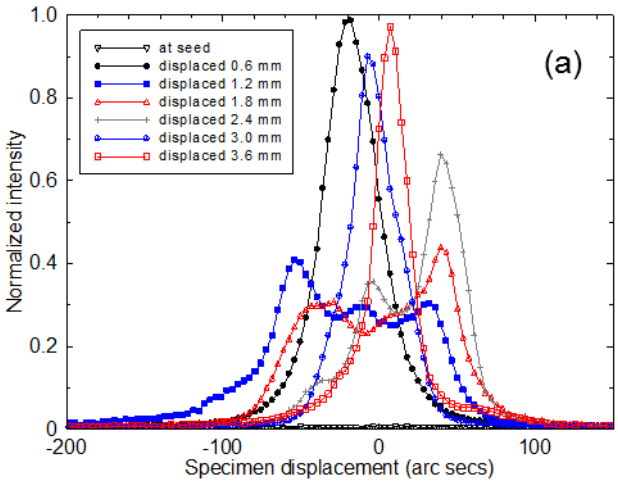
at seed
displaced 0.6 mm
displaced 1.2 mm
displaced 1.8 mm
displaced 2.4 mm
displaced 3.0 mm
displaced 3.6 mm
(a)
Normalized intensity
1.0
0.8
0.6
0.4
0.2
0
-200
-100
0
100
Specimen displacement (arc secs)

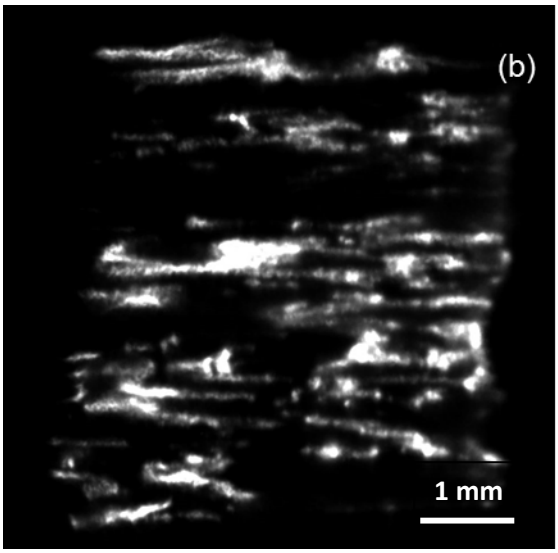
(b)
1 mm

Fig. 9

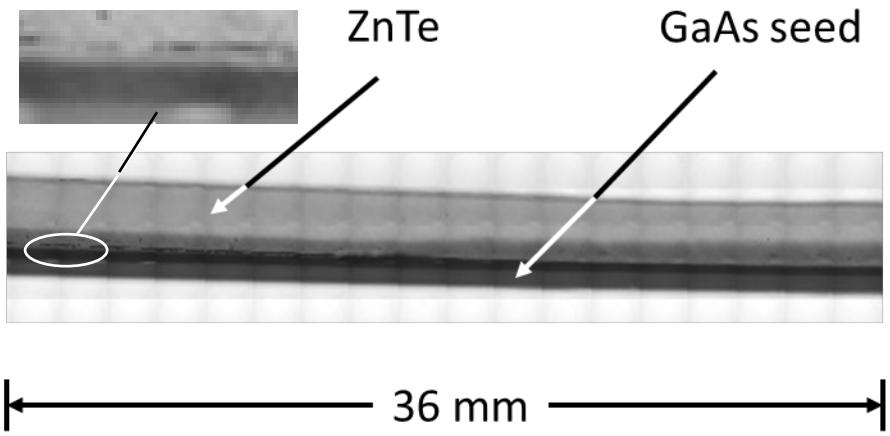

Fig. 10

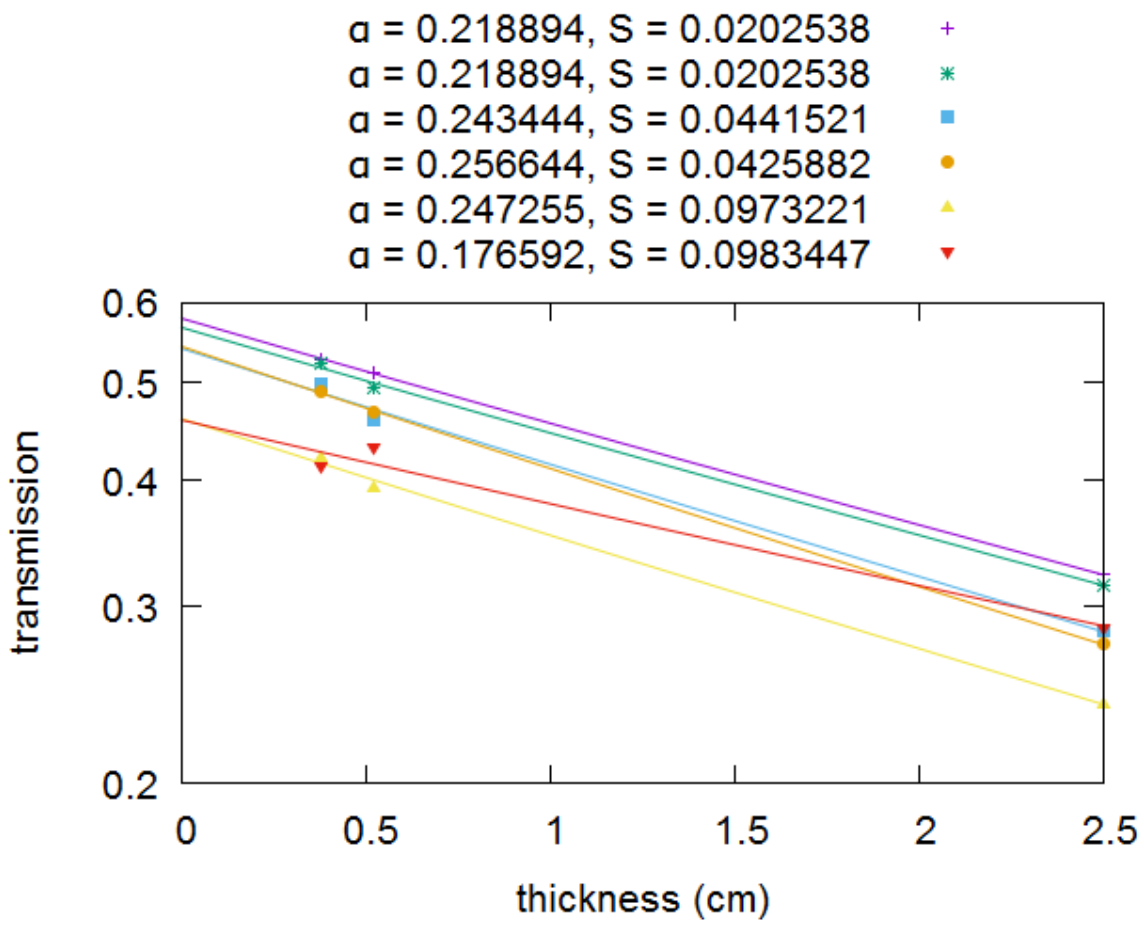
α = 0.218894, S = 0.0202538
α = 0.218894, S = 0.0202538
α = 0.243444, S = 0.0441521
α = 0.256644, S = 0.0425882
α = 0.247255, S = 0.0973221
α = 0.176592, S = 0.0983447
transmission
0.6
0.5
0.4
0.3
0.2
0
0.5
1
1.5
2
2.5
thickness (cm)

Fig. 11

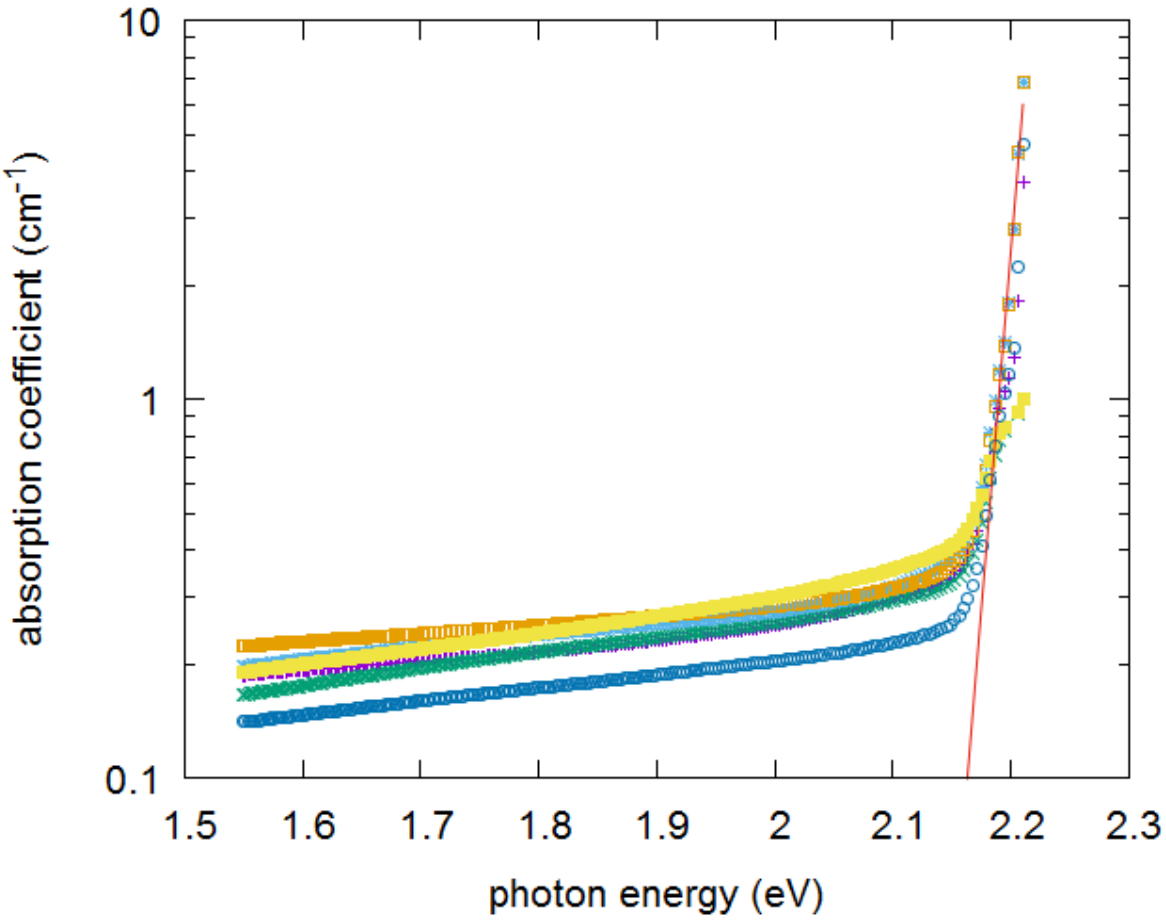
10
1
0.1
absorption coefficient (cm-1)
1.5
1.6
1.7
1.8
1.9
2
2.1
2.2
2.3
photon energy (eV)

Fig. 12

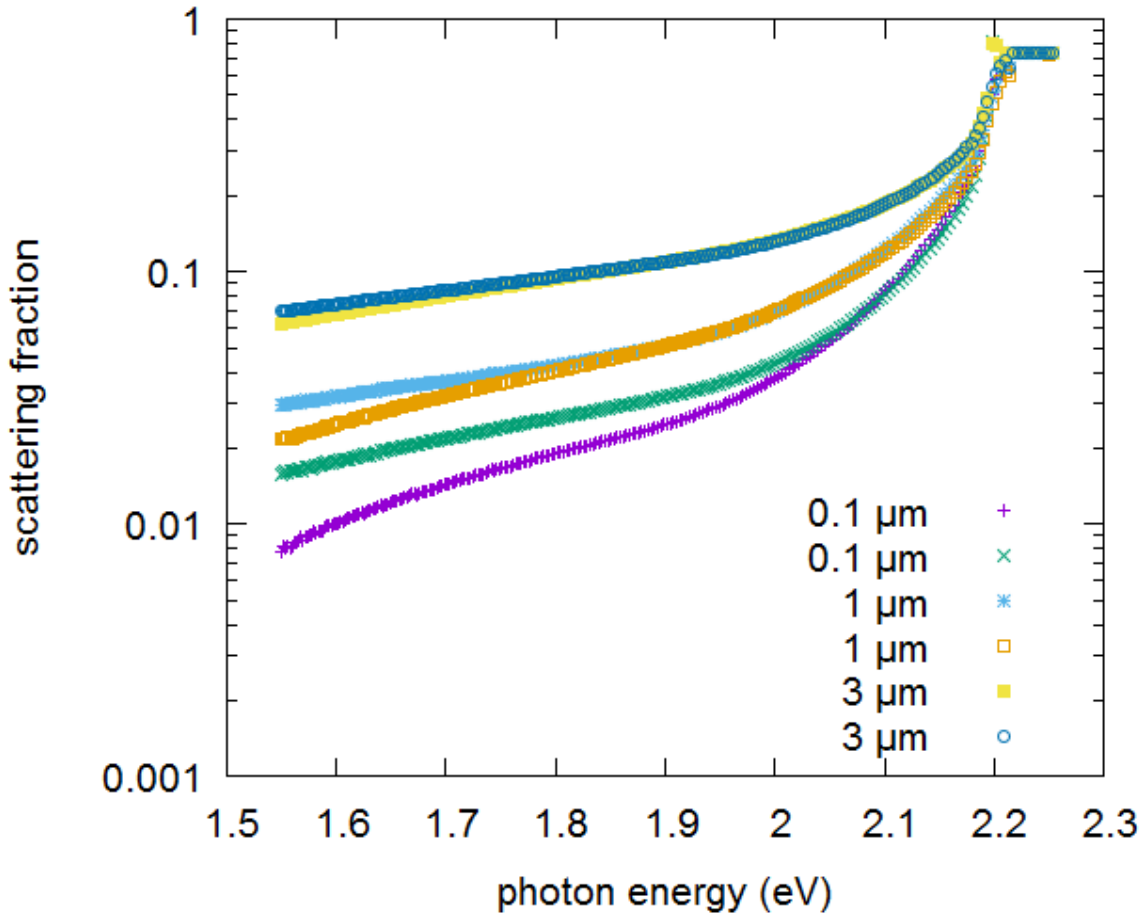
scattering fraction
1
0.1
0.01
0.001
1.5
1.6
1.7
1.8
1.9
2
2.1
2.2
2.3
photon energy (eV)
0.1 μm
0.1 μm
1 μm
1 μm
3 μm
3 μm

Fig. 13

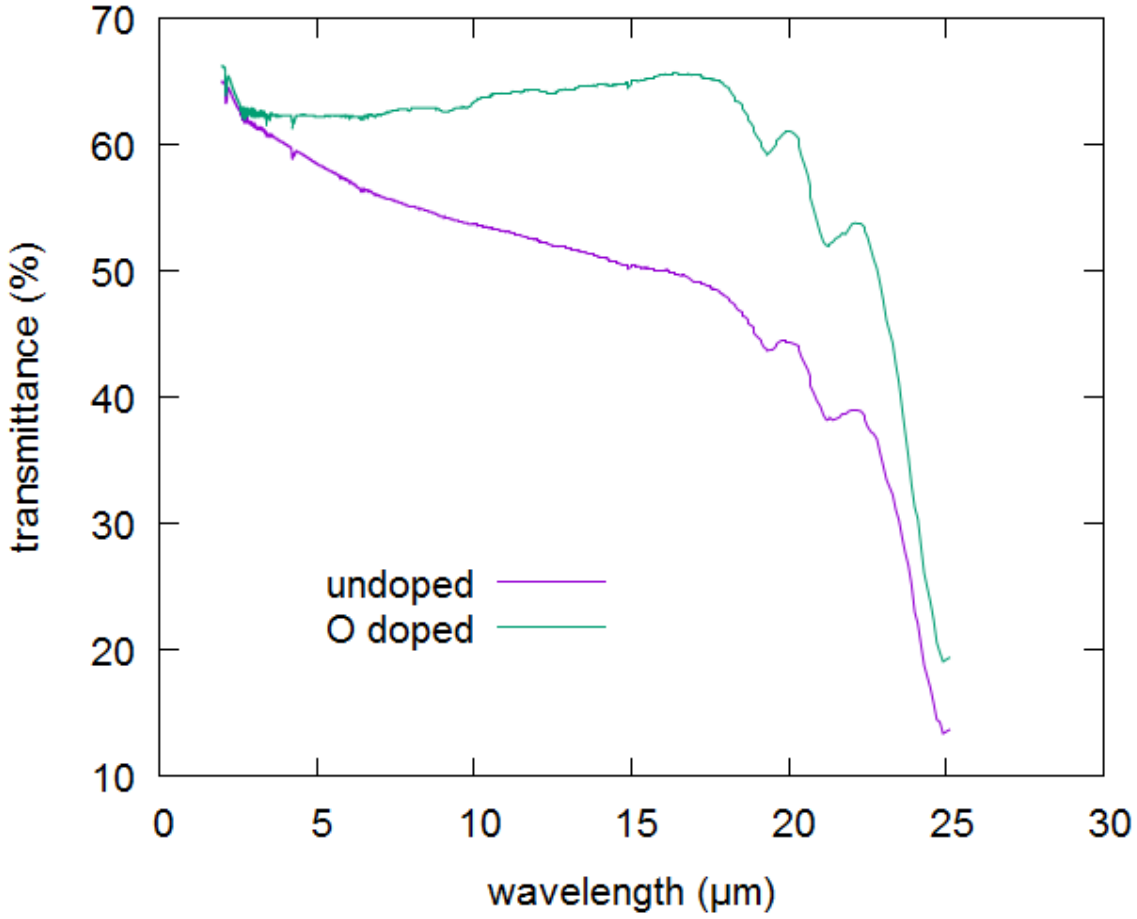
70
60
50
40
30
20
10
transmittance (%)
0
5
10
15
20
25
30
wavelength (μm)
undoped
O doped

Fig. 14

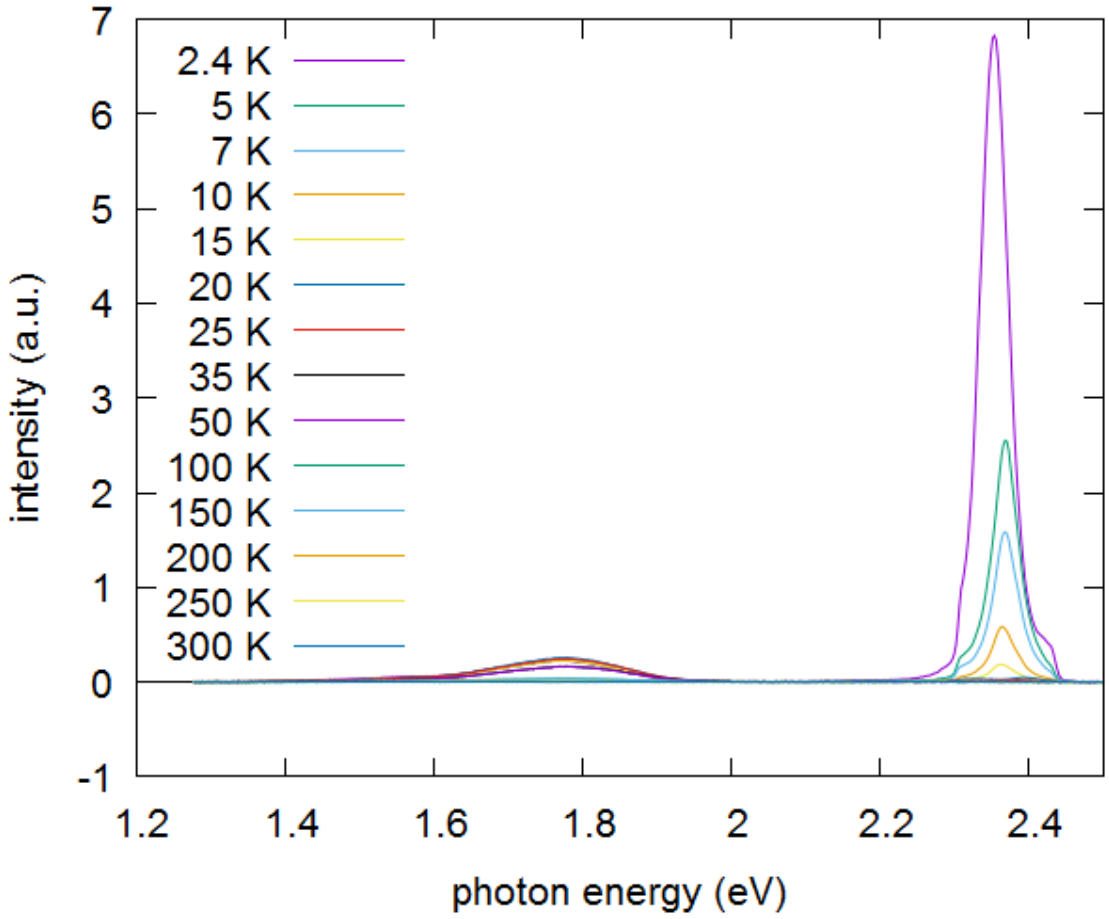
intensity (a.u.)
photon energy (eV)
2.4 K
5 K
7 K
10 K
15 K
20 K
25 K
35 K
50 K
100 K
150 K
200 K
250 K
300 K
7
6
5
4
3
2
1
0
-1
1.2
1.4
1.6
1.8
2
2.2
2.4

(a)

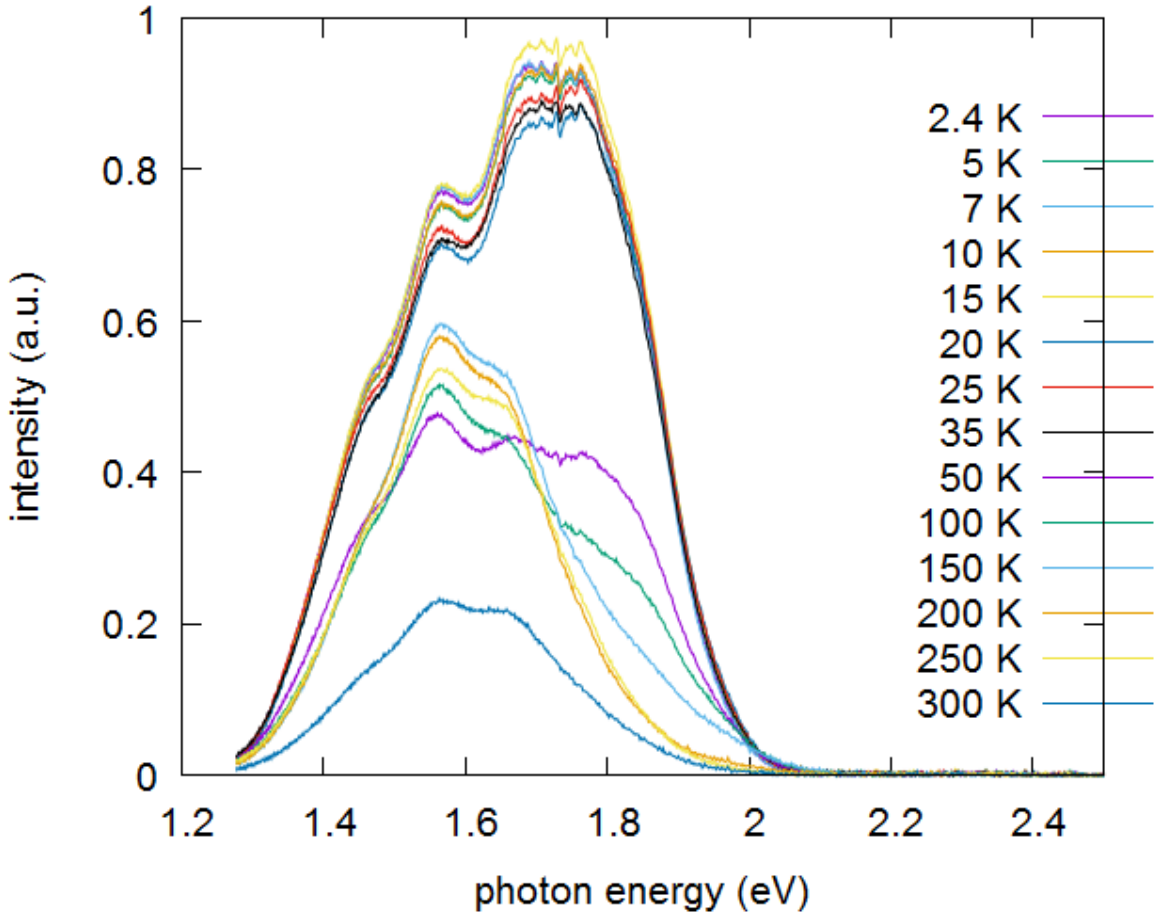
intensity (a.u.)
photon energy (eV)
1
0.8
0.6
0.4
0.2
0
1.2
1.4
1.6
1.8
2
2.2
2.4
2.4 K
5 K
7 K
10 K
15 K
20 K
25 K
35 K
50 K
100 K
150 K
200 K
250 K
300 K

(b)

Fig. 15

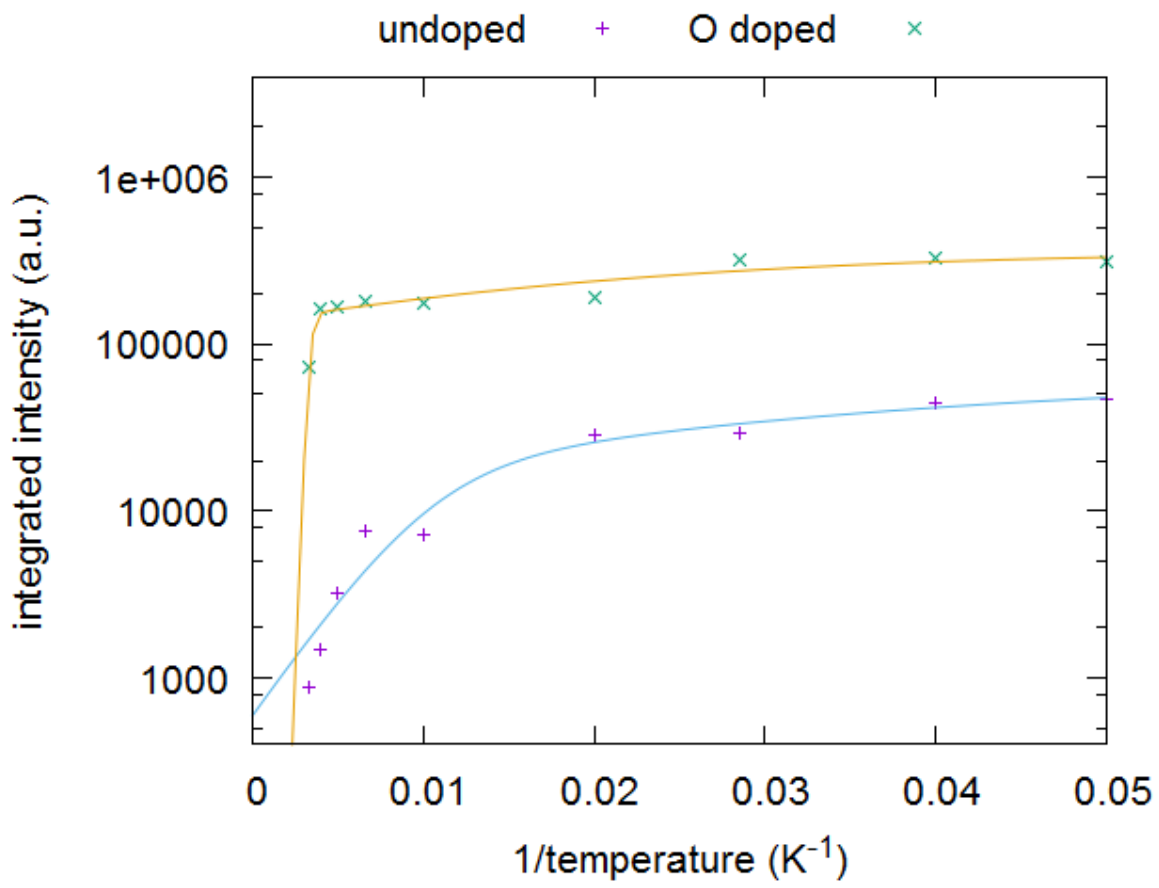
undoped
O doped
integrated intensity (a.u.)
1e+006
100000
10000
1000
0
0.01
0.02
0.03
0.04
0.05
1/temperature (K-1)

Fig. 16

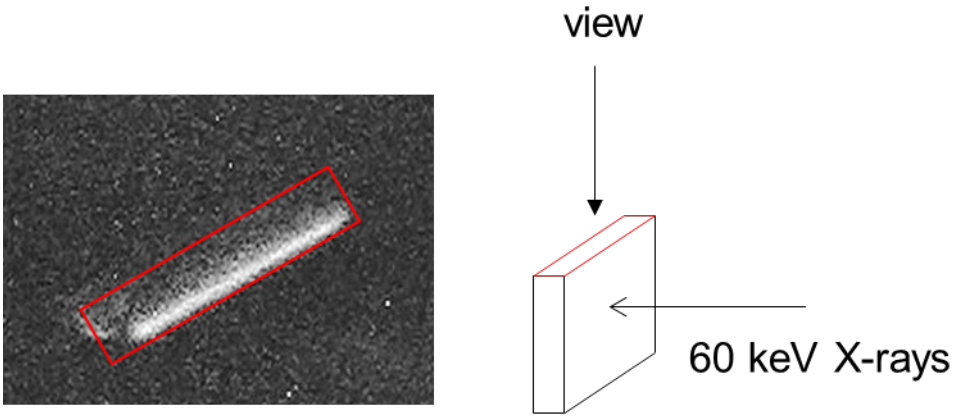

Fig. 17

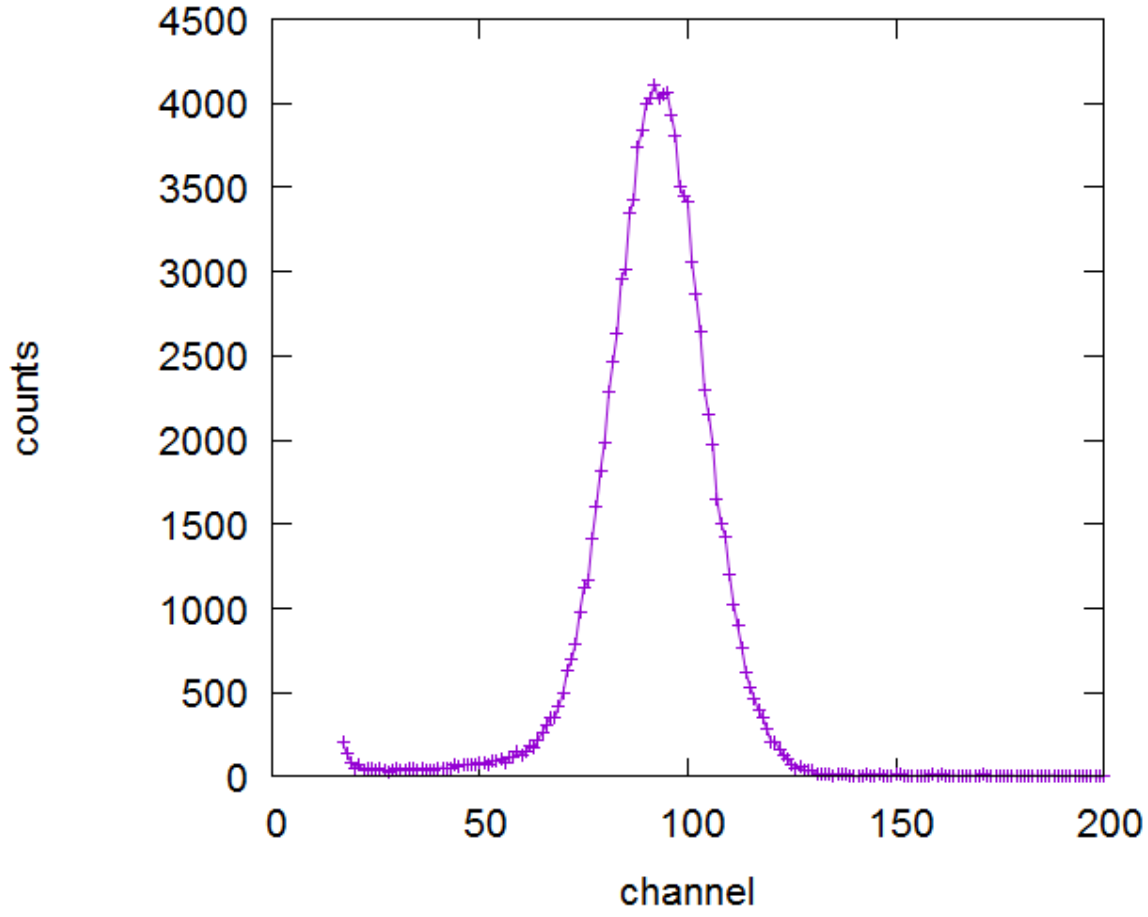
4500
4000
3500
3000
2500
2000
1500
1000
500
0
counts
0
50
100
150
200
channel